

Well Proximity Governing Stress Drop Variation and Seismic Attenuation Associated With Hydraulic Fracturing Induced Earthquakes

Hongyu Yu¹ , Rebecca M. Harrington² , Honn Kao^{1,3} , Yajing Liu⁴ , Rachel E. Abercrombie⁵ , and Bei Wang^{1,3} 

¹Geological Survey of Canada, Pacific Geoscience Centre, Sidney, British Columbia, Canada, ²Institut für Geologie, Mineralogie & Geophysik, Ruhr-Universität Bochum, Bochum, Germany, ³School of Earth and Ocean Sciences, University of Victoria, Victoria, British Columbia, Canada, ⁴Department of Earth and Planetary Sciences, McGill University, Montréal, Québec, Canada, ⁵Department of Earth and Environment, Boston University, Boston, MA, USA

Key Points:

- Stress drops of 484 hydraulic fracturing induced earthquakes ($M < 3$) are within the range observed for tectonic earthquakes elsewhere
- S-phase stress drop values estimated from spectral ratios are ~ 1 and 10 MPa for clusters proximal and distal to the well, respectively
- Lower stress drop values and higher attenuation proximal to the well may be due to higher pore pressure caused by injection

Supporting Information:

- Supporting Information S1

Correspondence to:

H. Yu and H. Kao,
hongyu.yu@rub.de;
honn.kao@canada.ca

Citation:

Yu, H., Harrington, R. M., Kao, H., Liu, Y., Abercrombie, R. E., & Wang, B. (2020). Well proximity governing stress drop variation and seismic attenuation associated with hydraulic fracturing induced earthquakes. *Journal of Geophysical Research: Solid Earth*, 125, e2020JB020103. <https://doi.org/10.1029/2020JB020103>

Received 1 MAY 2020

Accepted 28 JUL 2020

Accepted article online 2 AUG 2020

Abstract We use broadband seismic data collected within 3 km of a hydraulic fracturing (HF) well in northeast British Columbia, Canada, to estimate the stress drop values of HF-induced earthquakes and their spatial variation. Applying both spectral ratio and clustered single-spectra fitting methods to 484 induced earthquakes (M -1.0 to 3.0), we find that earthquakes close to the injection well have lower stress drop values than those at greater distance. Stress drop values are generally invariant within clusters either proximal (~ 0.1 –1 MPa) or distal (~ 1 –10 MPa) to the well, suggesting that dynamic ruptures in rocks with similar rheological properties tend to have relatively constant stress drop values. Clustered single spectrum fitting also suggests that the seismic quality factor (Q) is lower proximal to the well. We interpret the lower stress drop values and higher seismic attenuation proximal to the well as a result of higher fracture density and/or elevated pore pressure in the rock matrix due to hydraulic stimulation.

Plain Language Summary Earthquake static stress drop is the average difference in stress across the fault surface before and after an earthquake rupture. It is a measure of the stress released by fault slip. Investigating the stress drop of induced earthquakes helps us understand the causal relation between hydraulic fracturing (HF) and earthquake source properties. Here we study the source parameters of 484 HF induced earthquakes in the Montney Play of northeast British Columbia. We find that stress drop increases with distance to the injection well but is roughly constant within the respective proximal or distal groups of events. We also find that seismic energy loss during wave propagation (seismic attenuation) is higher near the well. The observations lead us to interpret that either the higher fracture density and/or elevated pore pressures near the well prevent the crustal rocks from storing and releasing larger magnitudes of stress at distances approximately < 1 km from the well.

1. Introduction

The Montney Play is one of the most active oil and gas production areas in Canada. Since the start of hydraulic fracturing (HF) activities in 2008, it has experienced a drastic increase of local seismicity, including three significant ($M_{4.5+}$) earthquakes (International Seismological Centre, 2019). While the large injected volumes of wastewater disposal (WD) are generally ascribed to M_{4+} induced events in the central and eastern United States (Ellsworth, 2013), it remains to be fully understood why the relatively low fluid injection volumes associated with HF in western Canada (e.g., Schultz et al., 2016; Wang et al., 2020), in Sichuan Basin, China (e.g., Lei et al., 2019) and recently in south Texas (e.g., Fasola et al., 2019) can lead to earthquakes of similar magnitude (e.g., Schultz et al., 2020; van der Elst et al., 2016). With intense injection operations and high levels of local seismicity, the Montney Play provides a natural laboratory to study the causal relation between HF and injection-induced earthquakes (IIEs) in detail (Mahani et al., 2017; Wang et al., 2020).

One approach to investigate the causal relation between HF and IIE is to measure the amount of stress release, that is, the stress drop, defined as the average stress difference across the fault before and after an earthquake rupture (Hanks, 1979). Fluid injection can perturb the local subsurface stress state through pore pressure diffusion and/or poroelastic stress transfer and thus induce ruptures along critically stressed faults

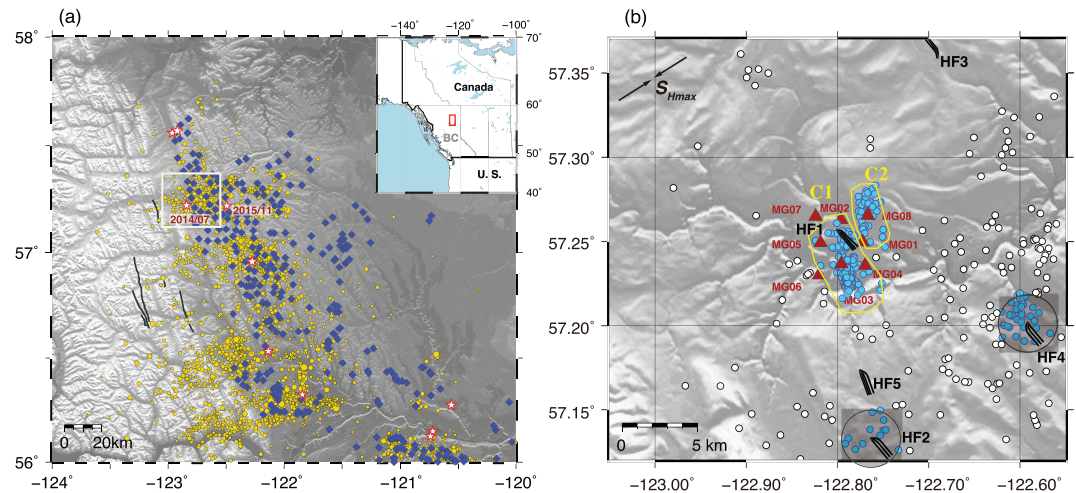


Figure 1. (a) Hydraulic fracturing activity and seismicity in northeast British Columbia, Canada. Blue diamonds: HF injection well pad distribution between 1 January 2014 and 31 December 2016, reported by the British Columbia Oil and Gas Commission. Yellow dots: 4,919 earthquakes for the same period cataloged by Visser et al. (2017). Stars: 10 M4–5 earthquakes that occurred between January 2008 and December 2018 (International Seismological Centre, 2019; Visser et al., 2017). Rectangle: 30 km × 30 km study area. Inset indicates the location of the Montney Play in BC. (b) Epicenters of 484 earthquakes with horizontal/vertical uncertainty smaller than 2 km, detected and relocated by Yu et al. (2019) and considered in this study. Turquoise/empty dots: earthquakes located within/further than 2 km to wellbores. Black lines: Map-view projections of horizontal well trajectories. Yellow curves approximately mark earthquake clusters (C1/C2) proximal to the HF1 well. Gray shaded circles enclose earthquakes located within 2 km of other active wells (HF2 and HF4) during the study period, which are excluded from the source parameter comparison of events proximal and distal to the HF1 wellbore.

(Scholz, 2019). The spatial variation of stress drop can highlight the heterogeneity in strength and possibly the hydrogeological properties of the fault zone, which is helpful to understand the underlying mechanism of IIEs. For example, a local decrease in stress drop could be an indicator of rupture along a weakened fault segment or where fault-fluid interaction may be more prominent (e.g., Chen & Shearer, 2013).

Whether a distinguishable difference exists between stress drop values of tectonic and induced earthquakes is still an open question (Zhang et al., 2016). Early studies suggested that IIEs may have lower average stress drop values (Abercrombie & Leary, 1993; Fehler & Phillips, 1991; Hough, 2014). While the relatively shallow focal depths of induced earthquakes might explain some of the observed lower values (Hough, 2014; Satoh, 2006; Zhang et al., 2016), the apparent lower stress drop may also be interpreted as an artifact of inadequate attenuation correction and/or the assumption of a constant rupture velocity over all rupture sizes (Tomic et al., 2009). The debate continues in recent studies applying spectral ratio methods that aim to remove path and site effects more effectively. For example, studies in two regions of the central and the eastern United States, respectively, suggest differences in stress drop values between tectonic and induced earthquakes that may become indiscernible within the context of the mode of faulting and earthquake depth (Boyd et al., 2017; Huang et al., 2017). Considering all the factors that may influence the estimate of stress drop (e.g., tectonic setting, seismic velocity, choice of source and station, seismic moment, and source model), it is hard to compare stress drop values derived for different regions. Instead, we focus our investigation on the spatial variation of stress drop in an area with relatively uniform seismogenic conditions. We compare the properties of earthquakes experiencing significant effects from HF injection proximal to the injection well and distal events experiencing less pronounced pore pressure and poroelastic stress changes, in efforts to determine the predominant controlling factor(s).

A closely related issue in the accurate determination of stress drop is constraining the effects of seismic attenuation, which is often parameterized via the seismic quality factor (Q). Adopting an appropriate Q value is particularly important when the corner frequency, and thus stress drop, is determined from fitting the single-event spectrum (Ko et al., 2012). Since Q is very sensitive to the mechanical properties of the host rocks, its spatial variation can also serve as an indicator on how HF injection affects the local stress state over the volume between seismic source and receiver.

In this study, we investigate the spatial variation of stress drop and seismic attenuation around an active horizontal HF well in the northern Montney Play (Figure 1). Yu et al. (2019) have compiled a detailed IIE catalog for our study area and reported that pore pressure diffusion is the predominant factor in controlling the IIE pattern immediately surrounding the wellbore (within ~ 1 km). Using the same catalog, we show that the typical values of stress drop of HF-related IIEs in close proximity to the wellbore is about one order of magnitude smaller than that of events at greater distances from the well. Hypocenters of low stress drop events also coincide with high seismic attenuation (lower Q values). Finally, we discuss the implications of our results for the seismogenic conditions of HF-related IIEs.

2. Data and Analysis

Our study area is situated in the Montney Play of northeast British Columbia (Figure 1a). Historical HF injection has been ongoing in this area since 2008, and seismic activity over the last decade has intensified. We analyze the source parameters of the 484 earthquakes ($M -1.0$ to 3.0) reported by Yu et al. (2019) in the northern Montney shale formation between 28 May and 15 October 2015, using ground motion recordings from a temporary deployment of eight broadband seismometers (Nanometrics Trillium Compact 20s, MG01–08; Figure 1b) at a sampling rate of 200 Hz. A total of five HF well pads (HF1–HF5) were stimulated during the study period (Figure 1b), among which HF1, HF2, and HF4 were correlated with increased local seismic activity. More details related to the respective injection volumes and operating times, as well as the correlated seismicity are provided in Yu et al. (2019). The observation period encompasses 6 weeks prior to and 3 months after treatments at HF1; all stations were located within 3 km from the well pad HF1. The small event-station distances (<3 km) provide high quality seismograms that allow the detailed investigation of source parameters of small-magnitude earthquakes presented here.

Single event spectra fitting retains the highest possible number of events and provides moment estimates. However, it includes the imprint of raypath attenuation and site effects that brings large uncertainties through the tradeoff between quality factor (Q) and corner frequency (Ko et al., 2012; Tomic et al., 2009). To improve the corner frequency estimates of single spectrum fitting, we investigate the spatial variation of Q values by clustering nearby events (section 2.1). We also refine corner frequency estimates using event spectral ratios and the method described in Wang et al. (2020), which is modified from the original approach (e.g., Hough & Dreger, 1995; Mori & Frankel, 1990) that corrects for travel path, site, and other non-source-related effects that can hinder robust corner frequency estimates (section 2.2). However, the spectral ratio fitting method only works for a small subset of events (or event pairs) that are collocated with distinguishable spectral ratios. A balance between the moment ratio and noise levels is required to allow resolvable differences in spectral corner frequencies (Huang et al., 2019). A good agreement between estimates from the clustered- Q single spectrum and spectral ratio corner frequency methods could further suggest the robustness of both refinement methods. Thus, we further use the spectral ratio estimates to check the robustness of optimal Q values constrained by clustered- Q spectral fitting. Finally, we assess stress drop estimates using the corner frequency from both estimates (section 2.3).

In addition to the fluid injection influences on host rock mechanic properties, we also investigate if the seismic attenuation is invariant with respect to the distance to the well. We do so by testing the assumption that the true Q value at distances beyond ~ 2 km from the well is the same as the corresponding Q value within 2 km. We use the observed spectral data to test if this is a valid assumption (section 2.4).

2.1. Estimation of Optimal Apparent Q Values Based on Clustered- Q Spectra Fitting

In the spectral fitting process, the effect of seismic attenuation is represented by the averaged Q value over the whole raypath (i.e., the apparent Q , hereinafter referred as Q). The clustered- Q fitting approach has been shown to produce better resolution on single spectrum fitting through robustly narrowing the Q value uncertainties (e.g., Ko et al., 2012). In this section, we take this approach to investigate the dependence of Q value as a function of distance to the well, as well as a function of depth. We subsequently fit the single-event spectra using the optimal Q value.

Following the definition of Yu et al. (2019), as shown in Figure 1b, the earthquakes could be divided into clusters located proximal to HF1 (C1 and C2) and distal to HF1. We therefore refer to events in C1 and C2 together as proximal events, whereas the remaining earthquakes outside of C1 and C2 are classified as

distal events. To avoid the possible contamination of induced events associated with ongoing injection at wells HF2–HF5, we exclude 49 events that occurred within 2 km distance of those wells (i.e., events within the gray circles centered at the well pads HF2 and HF4 in Figure 1b). A total of 435 events remain for source analysis. The average hypocenter distance of the proximal (C1 and C2) and distal events to MG stations are approximately 2.3 and 12.7 km, respectively. Yu et al. (2019) concluded that the stress state of the proximal cluster is largely affected by HF injection that induces a pore pressure change up to several MPa, whereas distal events experience limited or negligible stress perturbations from the injection at HF1. We further divide the two groups of events (proximal and distal) by hypocenter depth as 0–1, 1–2.8, and >2.8 km, shown in Figure 2a. This results in a total of six spatial groups for the clustered-Q single spectrum fitting approach: G1–G6. The depth limits applied for seismic vertical segregation are natural divisions between layers in the velocity model centered at (57.5°N, 122.5°W) (CRUST 1.0; Laske et al., 2013; Yu et al., 2019), considering Q depends on rock type (Toksöz et al., 1979) and is known to increase with depth (Abercrombie, 1997).

We begin with calculating the single spectrum fit by holding the Q value fixed at values ranging between 2 and 1,500 for each spatial group of earthquakes. We compute the single event displacement spectra using a multitaper spectral estimation on 1 s time windows for *P* and *S* phases starting 0.2 s before and 0.8 s after the phase arrival (Thomson, 1982). The short time windows prevent *S* phase energy being included in the *P* phase time window due to the short source-station distances. In addition, we calculate noise spectra for time windows of equal length starting 5 s before the *P*-phase arrival. We then fit the spectra using a Brune spectral model and a least squares curve fit (Abercrombie, 1995; Brune, 1970, 1971) (Equation 1). For a given value of Q (assuming Q is a frequency-independent constant), there are three free parameters in the spectral fitting: the long-period spectral amplitude (Ω_0), the spectral corner frequency (f_c), and high-frequency falloff rate (n),

$$\Omega(f) = \Omega_0 \frac{e^{-(\pi ft/Q)}}{1 + (f/f_c)^n} \quad (1)$$

where t is the travel time for the respective phases. The frequency band used for fitting is chosen where (1) the signal-to-noise ratio (SNR) exceeds 2 for each data point of the entire fitting frequency range, (2) the minimum and maximum fitting frequencies satisfy $0.5 \text{ Hz} \leq f_{min} \leq 5 \text{ Hz}$ and $10 \text{ Hz} \leq f_{max} \leq 80 \text{ Hz}$, respectively, and (3) the entire bandwidth is larger than 20 Hz ($f_{max} - f_{min} \geq 20 \text{ Hz}$).

Next, we perform a grid search for the optimal Q values with the lowest root-mean-square (RMS) misfit averaged over a given group. Within the group, the RMS value of each event is the mean of the constrained records from all the stations. The RMS value of a single record is obtained from the respective fitting width of the frequency band (i.e., where $\text{SNR} \geq 2$). We apply two quality control criteria, as (i) only considers a single spectrum fit with the RMS value ≤ 1 as a valid fit and throws away all the fits with the RMS values > 1 , and (ii) for a given cluster Q value, at least 10 events are required to calculate the corresponding mean RMS misfit. The optimal Q value of each group is found when the RMS misfit is minimal (Equation 2):

$$(Q_i, \text{RMS}_i)_{optimal} = \min_{2 \leq Q \leq 1500} \sum_{j=1}^{N_i} \text{RMS}(Q, \text{event } j), \quad (2)$$

where N_i is the number of events in group i (where $i = 1, \dots, 6$).

Sometimes, the RMS misfit of the optimal Q is larger than the neighboring values as a result of it containing a larger number of fitted records. An extra fitted event could lead to a higher mean RMS misfit within a cluster, thus potentially leading to a differing (or improper) Q value due to a fewer number of events and smaller RMS values. To address potential problems of different optimal Q values arising from varying numbers of events within the same group, we use the fitted number of events for the initially selected Q as the upper limit of event number in group i ($N_{i,max}$). For Q values that can be fit by a larger number of events, we use only the $N_{i,max}$ events with the smallest RMS values and then update the averaged RMS misfit to reselect the optimal Q. Figure 3 demonstrates the improvement of clustered-Q spectral fitting compared to regular single-event spectral fitting with an assumed Q value (Abercrombie, 1995).

Once we constrain the best Q for a given cluster, we then use it for all events within the cluster to obtain the corresponding values of Ω_0 and f_c . We calculate values of seismic moment (M_0) using the following equation (Brune, 1970, 1971),

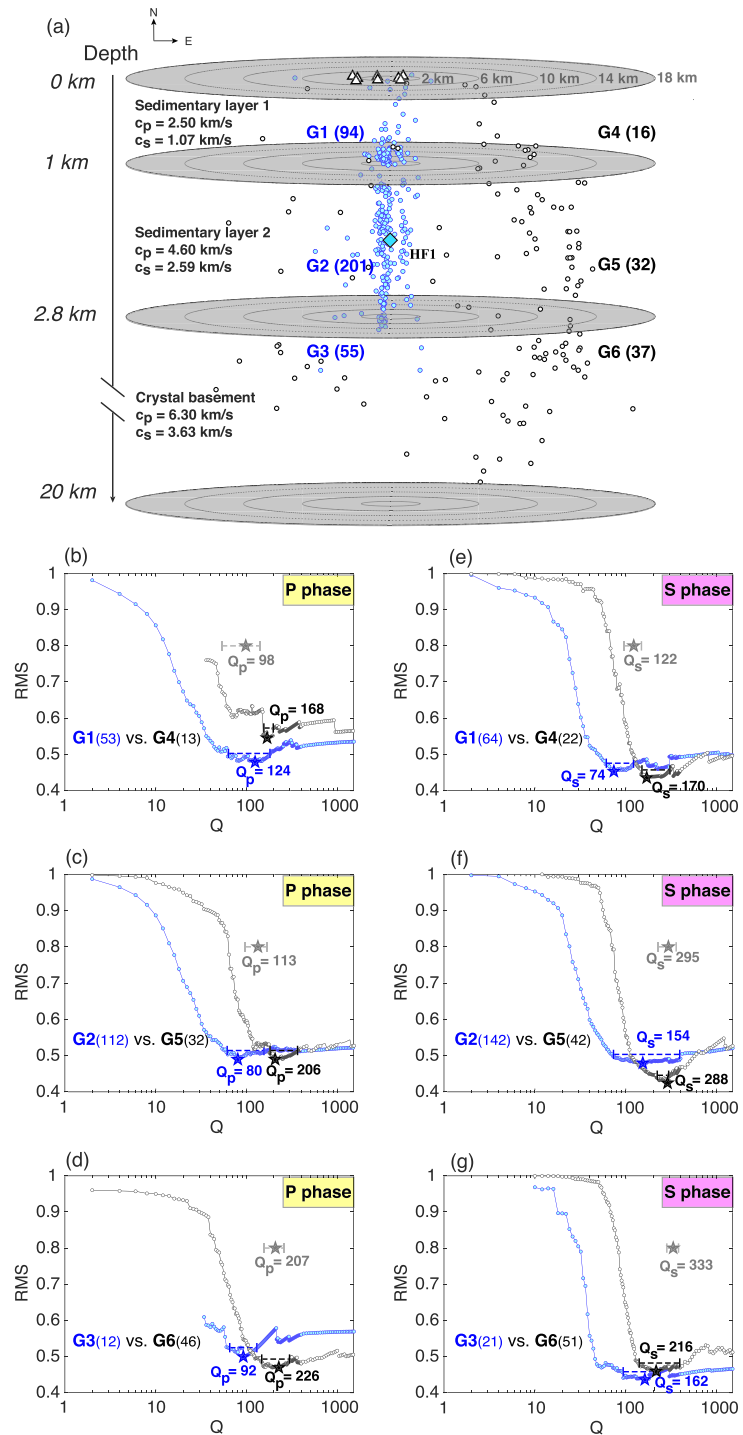


Figure 2. Optimization of seismic quality factor (apparent Q). (a) Schematic diagram of event spatial grouping used for clustered- Q estimation (G1–G6): Earthquakes are grouped into three depth layers, at 0–1, 1–2.8, and >2.8 km, based on the velocity model (Laske et al., 2013). The number of earthquakes in each group is marked in brackets. Note the varying horizontal and vertical aspect ratio. Events within C1/C2 indicated by blue dots (proximal groups: G1–G3); events at greater distance indicated with black circles (distal groups: G4–G6). (b) RMS misfit variation resulting from single spectrum fits of P phase for each assumed Q of clusters G1/G4 (with values of $N_{i,max}$ marked on the side). RMS values are averaged over all events within a given cluster (see text). Blue/black stars mark the optimal apparent Q values of clusters G1/G4. Horizontal dashed lines: 5% variation of minimum RMS value. Gray star with error bars: value of theoretical Q_4^{model} (see section 2.5). (c and d) Same as (b) for focal depths between 1–2.8 and >2.8 km, respectively. (e–g) The same as (b–d) but for S phases.

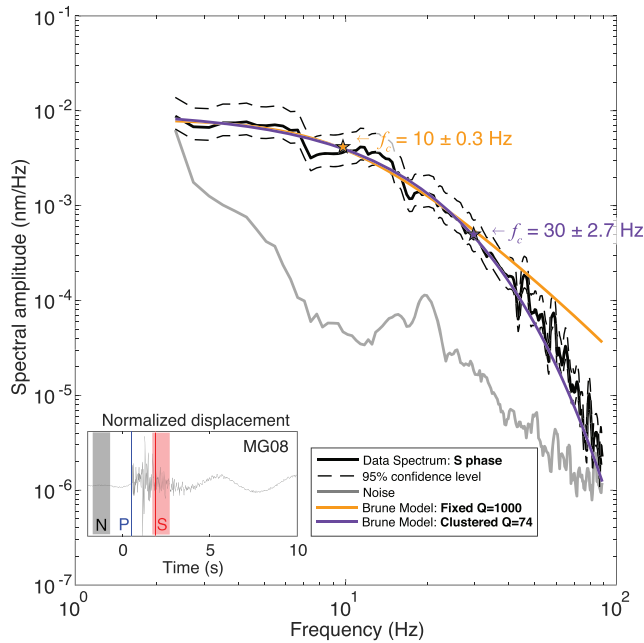


Figure 3. Example of single spectrum fits between assumed constant Q (orange) and clustered- Q fitting (purple) for an M 0.2 event on 2 August 2015 at 11:45:32. Inset: Normalized displacement of the event. Blue/red vertical lines mark the arrival of P/S phase. Gray/red shaded area: 1 s time window for noise/ S phase signal. The clustered- Q value is 74 and leads to a corner frequency of 30 Hz, compared with the estimate of 10 Hz obtained with an assumed $Q = 1,000$.

is relatively low compared to other studies (e.g., Abercrombie, 2015; Huang et al., 2016), the corner frequency estimation is considered stable when the CC threshold is set in the range between 0.7 and 0.85 (Abercrombie et al., 2017; Ruhl et al., 2017). We also test a higher CC threshold of 0.8, with similar results, but the higher CC led to fewer available event pairs and thus fewer stress drop estimates. We therefore opt to use a threshold of 0.7 and ensure robustness of the fitting by setting additional strict quality control criteria after event pair selection. Second, the event pair have hypocentral distances of less than 5 km, given the location uncertainty of 2 km. We note that 54% of qualified event pairs are within a hypocentral distance of 1 km and 77% within 2 km for the P phase. For the S phase, the percentages are 44% and 75% for hypocentral distances within 1 and 2 km, respectively. Third, the event pair has a magnitude difference larger than 0.5, attributed to the low noise level because of close event-station distances. Finally, their low-frequency amplitude ratio should be larger than 2. The last two criteria for selecting event pairs listed above help ensure resolvable differences in spectral corner frequencies between the two events. The fitting frequency band is determined with the same criteria applied for single spectrum fitting. The criteria to find event pairs are the first step of event selection, and we try to avoid removing too many event pair candidates before knowing if there are resolvable differences in corner frequency. Additional quality control criteria (introduced later) we applied to ensure the robustness of our spectral ratio fitting include a second check on the fitting quality.

For pairs recorded by multiple stations, we calculate the station-average spectral ratio by stacking single-station spectral ratios, applying the narrowest frequency band for which the SNR requirement is satisfied among the averaged records (Figure S1b in the supporting information). Second, we fit the corner frequencies of both the master and eGf events with the theoretical expression of the spectral ratio assuming a Brune spectral model (Brune, 1970, 1971) as

$$\frac{\Omega_1(f)}{\Omega_2(f)} = \frac{M_1}{M_2} \left(\frac{1 + \left(\frac{f}{f_{c2}}\right)^2}{1 + \left(\frac{f}{f_{c1}}\right)^2} \right) \quad (4)$$

where M_1 and M_2 are seismic moment of the master and the eGf events, respectively. Considering the estimated seismic moment values (M_1 and M_2) based on clustered single spectra fitting are well determined,

$$M_0 = \frac{4\pi\rho c^3 R \Omega_0}{U_{\phi\theta}} \quad (3)$$

where density, ρ , is set to 2,790 kg/m³, velocity c for P and S waves is chosen according to the value in the velocity model at the focal depth of respective event (Figure 2a), and R is the hypocentral distance. The mean radiation pattern, $U_{\phi\theta}$, is set to be 0.52 and 0.63 for P and S waves, respectively (Aki & Richards, 1980).

The apparent Q values applied here represent the averages over the whole raypath. The differences of measured apparent Q values for different clusters do not necessarily reflect a true Q -value contrast. That is, the larger apparent Q values of the events distal to the well could possibly be a path effect due to longer wave propagation in the deeper, higher Q layers. Because of the potential averaging effect, we will further evaluate the spatial variation of true Q values in section 2.4.

2.2. Determination of Corner Frequency Based on Spectral Ratio Fitting

We calculate the spectral ratio of collocated event pairs recorded at a common station using a smaller event (empirical Green's function, eGf) and a larger event (master event). A suitable event pair needs to satisfy four criteria. The first and most decisive criterion is that the cross-correlation coefficient (CC) of the waveform pair in a 6 s length time window exceeds 0.7, where the similarity of the whole waveform implies collocation. Specifically, we cross-correlate waveforms 3 s before and after S arrival to include P and S together, using a band-pass filter between 1 and 20 Hz. While the CC threshold here

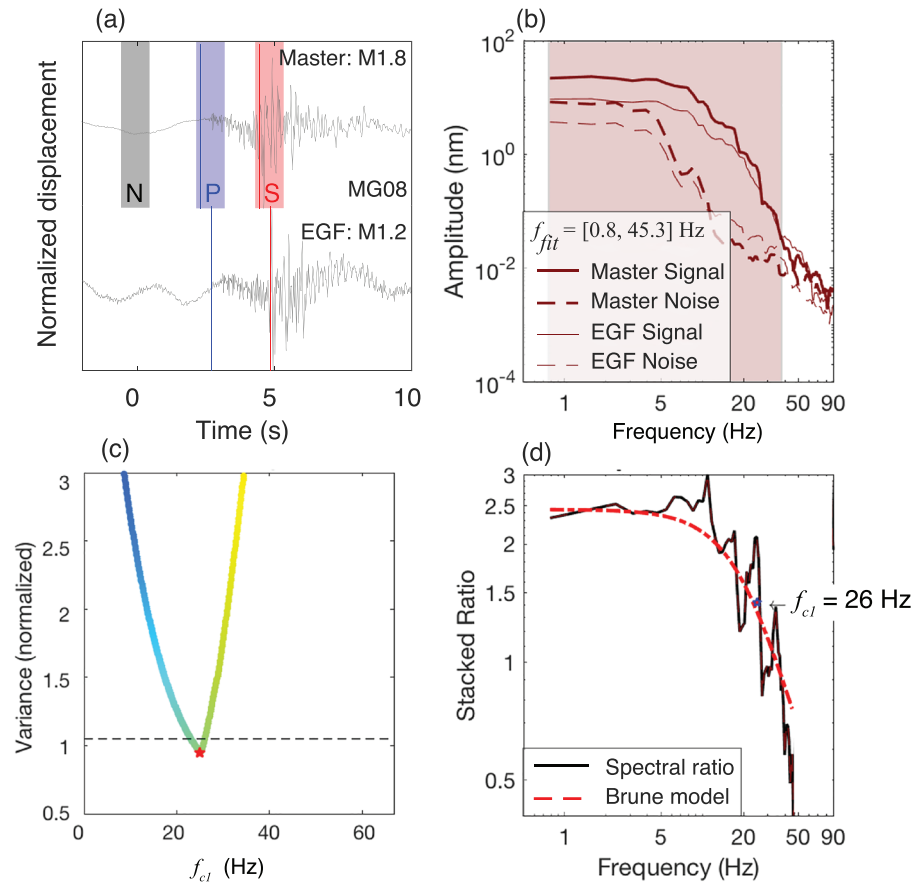


Figure 4. Spectral ratio fitting example from a pair of events that occurred on 13 September 2015 03:10:16 (M1.8) and 18 August 2015 01:33:49 (M1.2). (a) Normalized displacement of the two events in the pair. Blue/red vertical lines mark the arrival of *P/S* phases. Gray/blue/red shaded area: 1 s time windows for noise/*P/S* phase spectral estimations. (b) Single spectrum for noise (dashed line) and *S* phase (solid line) of the master event (thick line) and the eGf (thin line), respectively. Red shaded area: fitting frequency band. (c) Variance of spectral ratio fitting for different values of corner frequency for the master event f_{c1} . Dashed line: 5% increase of fit variance. Star: the optimal f_{c1} . (d) Comparison between the spectral ratio of the event pair (black solid line) and Brune model fit (red dashed line), based on the optimal f_{c1} obtained in (c).

we narrow the variance of M_1/M_2 up to 1% of the initial value during the fitting process, to improve the solution of corner frequencies (f_{c1} , f_{c2}). We further evaluate the uncertainty of estimated f_{c1} (δf_{c1}) using the range where fit variance increases by 5% (Viegas et al., 2010). The fit variance is defined as the curve-fitting residual normalized by the ratio of M_1 and M_2 . We require the fit to pass two quality control criteria in order to consider it robust: (1) the RMS value must be smaller than 0.6 and 0.3 for *P* and *S* phases, respectively (a larger RMS criterion for *P* phases is due to the lower SNR relative to *S* phases), and (2) $\delta f_{c1}/f_{c1}$ must be smaller than 1 (to guarantee the fit is sensitive to f_{c1}). Among event pairs that satisfy the criteria, we also manually remove cases with qualitatively poor f_{c1} and f_{c2} fits resulting from the oscillation of spectral ratios at high frequencies. Finally, we calculate the weighted f_{c1} for one master event with several eGfs based on inverse-variance weighting following Abercrombie et al. (2017). Figures 4 and S1 show two representative examples with different magnitudes to illustrate the spectral ratio procedure and the quality of spectral ratio fits.

As corner frequencies estimated from spectral ratio fitting are considered more robust than those estimated with clustered-Q spectral fitting, we also use them to verify the estimated apparent *Q* values in section 2.1. A spectrum could be expressed as the product of source, site, and path effects, and the apparent *Q* only involves the path effect. We first remove the source effect by dividing the recorded spectrum with the modeled source spectrum, using the corner frequencies estimated from spectral ratio fitting. The source spectrum described by Brune (1970, 1971) is written as

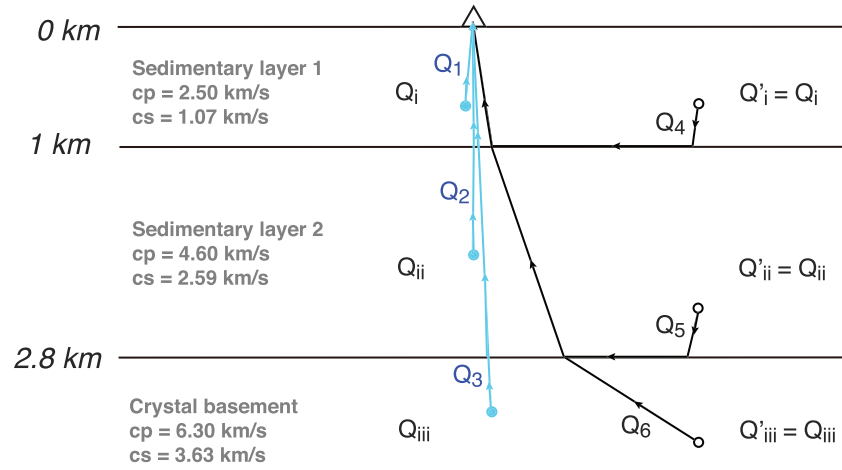


Figure 5. A schematic diagram of the Q-test Model 1 to determine if a horizontally varying Q is necessary to explain the observations of lower Q values near the well bore, or if refracted raypaths through high-Q layers for distal earthquakes is sufficient (see text). Q_1 – Q_6 is the apparent Q of representative travel paths for each earthquake group presented in Figure 2. The true Q values in close proximity to the injection well are marked as Q_i , Q_{ii} , Q_{iii} , and as Q_i' , Q_{ii}' , and Q_{iii}' at greater distances.

$$A_0(f) = \frac{\Omega_0}{1 + (f/f_c)^2} \quad (5)$$

The residual spectra should only contain the propagation and site effects. We further remove the site effect by calculating the ratio of the residual spectra of two master events recorded by the same station, presumably one from the cluster proximal to the HF wells (G1–G3) and the other one from the more distal cluster (G4–G6). We then compare the residual spectral ratio with the ratio of their geometrical spreading factors $\frac{e^{-(\pi f t_{ds}/Q_{ds})}}{e^{-(\pi f t_{pr}/Q_{pr})}}$, where the wave travel times (t) and the apparent Q values along the propagation paths of the two events are applied respectively (i.e., ds for distal and pr for proximal). An example of consistency between the S phase f_c estimated from spectral ratio and the apparent Q values constrained by clustered-Q spectra fitting is shown in Figure S2.

2.3. Stress Drop Estimation

Based on a circular crack model (Eshelby, 1957), we use the seismic moment estimated from low-frequency spectral amplitude and both the clustered-Q spectra and spectral ratio fits of corner frequency to calculate the stress drop ($\Delta\sigma$) after converting corner frequency to source radius r (Madariaga, 1976):

$$r = \frac{kc}{f_c} \quad (6)$$

$$\Delta\sigma = \frac{7M_0}{16r^3} \quad (7)$$

where k is a constant related to the reciprocal relation between f_c and r is set as 0.25 and 0.32 for P and S waves, respectively, by assuming a rupture velocity $c = 0.9c_s$ (c_s is the shear wave velocity) (Huang et al., 2016; Imanishi et al., 2004; Kaneko & Shearer, 2015; Sato & Hirasawa, 1973).

2.4. Variation of True Q With Distance

In order to verify the necessity of the lateral variation of true Q values, we design a test assuming that the true Q value is constant along horizontal distance to the well bore (Model 1; Figure 5) and then compare the forward-modeled apparent Q values with the observed ones. If the theoretical apparent Q values are comparable with observed Q, the difference of apparent Q between proximal and greater distance is attributed to the long-distance refracted raypath traveling along the lower layer. Alternatively, if the horizontal constant

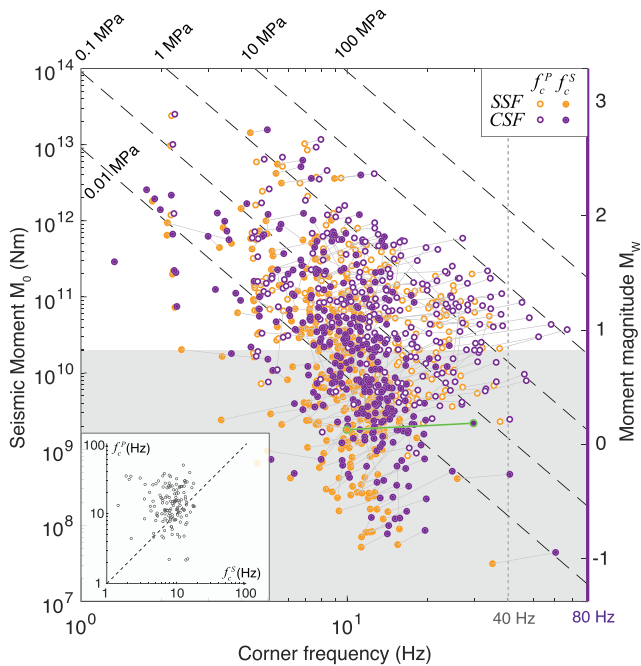


Figure 6. Scaling between corner frequency (f_c) and seismic moment (M_0) based on single spectra fits. M_0 here is uniformly estimated from low-frequency amplitude (Equation 3). The uncertainty of moment magnitude estimation ($M_w = \frac{2}{3} \log_{10}(M_0) - 6.073$; Kanamori, 1978) is ± 0.2 at the 95% confidence level. f_c estimates use Orange empty/filled circles: single spectrum fitting (SSF) based on P/S phases. Purple empty/filled circles: clustered-Q spectra fitting (CSF) based on P/S phases. Gray shaded area: unreliable fits due to bandwidth limitations of events with $M_0 < 2 \times 10^{10}$. Event pair highlighted in green: example of spectral fit comparison shown in Figure 3. Inset: Comparison between CSF estimates of f_c^P and f_c^S for the same events with $M_0 < 2 \times 10^{10}$. Dashed line: reference for $f_c^P = f_c^S$.

theoretical apparent Q values are not consistent with the observed Q values, it would suggest that the aforementioned factor cannot fully explain the apparent Q difference and that there must be horizontal variation of true Q.

Specifically, we assume a layered Q model consistent with the local velocity model (Figure 5). We only consider recordings of proximal events with direct raypaths and distal events with refracted raypaths as the first arrival. The relation between Q values and travel time can be written as in Table S1. We first resolve nonnegative linear least squares solutions of Equations S1–S3 to obtain the true Q value, together with the assumption that true Q values proximal to the well (Q_i , Q_{ii} , and Q_{iii}) are identical to those at greater distances (Q_i' , Q_{ii}' , and Q_{iii}'), as shown in Figure 5. We then calculate the theoretical apparent Q values at greater distance through Equations S4–S6 (Q_4^{model} , Q_5^{model} , Q_6^{model}) and compare them with observed ones (Q_4^{obs} , Q_5^{obs} , Q_6^{obs}).

We apply the forward calculation to both P and S phases. As a result, we have 359 and 751 equations for resolving true Q values for P and S phases, respectively, and 179 (P) and 248 (S) equations to estimate the theoretical Q_4^{model} , Q_5^{model} , and Q_6^{model} values. The test results are marked with gray symbols in Figures 2b–2g. The normalized residual of true Q values is 0.01 and 0.09 for P and S phases, respectively. The larger residual of S phases may be due to the differing choice of optimal apparent Q (Figure 2) or that the S wave velocity model is not as accurate as the P wave model (e.g., in the case of an erroneous assumption of a Poisson solid, as a result of fluid injection and/or concentrations of fractures and elevated fluid pressures).

We note that the layered Q model may not be a unique solution to explain the apparent optimal Q data set. An alternative simple homogeneous model with a thin, low Q, top layer, would also viably fit the data. However, the latter model would be less consistent with independent information on the local geological setting and would be

inconsistent with the local velocity model (Figure S3, Table S2, and Text S1). It is the consideration of independent evidence, such as the geological setting and the stress drop distribution that enable us to favor the layered Q model. We expand on this discussion further in section 4.

3. Results

3.1. Optimal Apparent Q and Single Spectrum Fitting

As shown in Figure 2, clustering results from single spectrum fits based on the P and S waveforms consistently prefer lower Q values in groups proximal to HF1 (G1–G3) compared to greater distance (G4–G6). Averaged ratios (Q_{prox}/Q_{dist}) based on P and S phases estimations are ~ 0.51 and ~ 0.57 , respectively. If we consider the 5% variation of minimum RMS misfit as the acceptable Q interval, the range could be quite wide, especially for S waves at depths > 1 km (Figures 2f and 2g). Even though we are not able to efficiently constrain the optimal Q here, the point of this comparison is to prove the necessity of applying different Q values during clustered-Q spectrum fitting for proximal versus distal events to the well, which is supported by the easily distinguishable curve patterns followed by the two spatial groups (open blue circles vs. open black circles in Figure 2).

By adjusting the single spectrum fits using the optimal Q values, we estimate corner frequencies for 231 and 296 events out of the 435 events using P and S phases, respectively (Figure 6). The mean value of f_c^P/f_c^S is ~ 1.2 , which is consistent with result from recent studies using the spectral ratio approach (Abercrombie et al., 2017; Ruhl et al., 2017) and also with the modeling of Kaneko and Shearer (2015). The overall

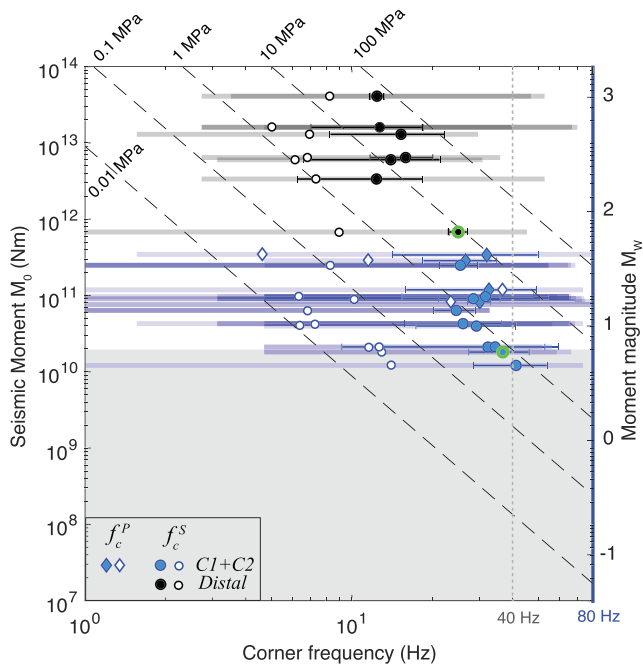


Figure 7. f_c estimates using spectral ratio fitting. Filled blue diamonds: f_c estimates of distal events using spectral ratio fitting (SRF) based on P phases. Filled blue/black circles: SRF estimates of proximal/distal events based on S phases. Error bars are estimated from the frequency bandwidth 5% increase variance of fit (Viegas et al., 2010). Transparent bars: frequency band used for SRF. Empty diamonds/circles: estimates from CSF of the same events constrained by spectral ratio fitting. Examples of spectral ratio fits highlight in green are shown in Figures 4 and S1. Dashed lines: stress drop reference based on S phases with $c_s = 2.59$ km/s (Equation 7).

comparison between regular single spectrum fitting and clustered-Q fitting is shown in Figure 6. Generally, fitted f_c values are consistently higher after clustering, and the upper limit of resolved f_c increases from 40 to 80 Hz (80% of Nyquist frequency; Shi et al., 1998; Viegas et al., 2010). The maximum stress drop value according to clustered-Q fitting reaches ~ 10 MPa. We notice a relatively smaller f_c correction by Q-value clustering upon S phase estimates compared to P phases. It is possibly due to the less well-constrained optimal Q_S values for the two lower layers (Figures 2f and 2g), as the overestimation of Q_S would result in underestimated f_c values (Ko et al., 2012). Abercrombie et al. (2017) and Ruhl et al. (2017) report that the f_c estimates would be biased on the low side when its value is beyond approximately one half to two thirds of the maximum resolvable frequency ($f_{res} = 80$ Hz), meaning we may not robustly resolve corner frequencies that are above 40 Hz. If we consider an earthquake that occurred near the well, at typical depths of ~ 2 km, the maximum resolvable f_c value is 40 Hz. To resolve a stress drop down to 1 MPa, the smallest moment we can constrain would be 2×10^{10} Nm (i.e., $M_W 0.8$; Equation 7). For smaller events with $M_W < 0.8$, marked as the gray shaded area in Figure 6, the almost constant f_c value (~ 10 – 20 Hz) may be an artifact of solutions trapped in local minima due to the fitting frequency band not being broad enough to cover the true (higher) f_c . The fact that two exceptional events below the $M_W 0.8$ threshold but with relatively higher SNR have corrected larger f_c values of 40 and 60 Hz also seems to suggest that the remaining low f_c values are not reliable. Thus, to avoid interpreting artifacts derived from bandwidth resolution at higher frequency as real source effects, we only consider events with $M_W > 0.8$. The median stress drop value for P phase estimates is 0.08 MPa, with a log standard deviation of 0.8 (in the unit of \log_{10}), and the median value of S phase estimates is 0.03 MPa, with a log standard deviation of 0.7.

The low median values relative to earthquakes of tectonic origin result from the relatively larger number of events proximal to the well bore, which have lower stress drop values compared to the more distal events (177 vs. 91 resolvable P phases and 227 vs. 115 resolvable S phases for events proximal and distal to the wellbore, respectively). We note that a considerable portion of P phase stress drop estimates are on the order of ~ 10 MPa, as shown in Figure 6. The variation of stress drop values is up to ~ 1.5 orders of magnitude. The large range of stress drop values observed here compares with other IIE studies (e.g., Goertz-Allmann et al., 2011; Kwiatek et al., 2014) and could be related to the larger distance scale (up to ~ 10 km) over which the earthquakes occur. The fact that the magnitude of the stress drop correlates with the distance to the well again supports the observation of the stress drop difference between two clusters as being statistically significant.

3.2. Stress Drop Distribution From Spectral Ratio Fitting

We are able to estimate the corner frequencies of 4 and 17 master events (the larger event of a spectral ratio pair) based on P and S phases, respectively. Constrained events with fitted frequency ranges are shown in Figure 7. All four events with P phase measurements are within 1 km of HF1, so we use the S phase measurements to investigate the spatial distribution of stress drop. The S phase corner frequency values range from 12 to 41 Hz, and seismic moment ranges between 10^{10} and 10^{14} Nm. The static stress drop values inferred from the estimates of M_0 and f_c range between 0.7 and 21.9 MPa. The stress drop values are comparable to that of tectonic earthquakes with similar magnitudes (Abercrombie, 1995; Shearer et al., 2019; Ye & Ghassemi, 2018) and overall lower than values of IIE observed in other regions of the WCSB (Clerc et al., 2016; Holmgren et al., 2019; Zhang et al., 2016).

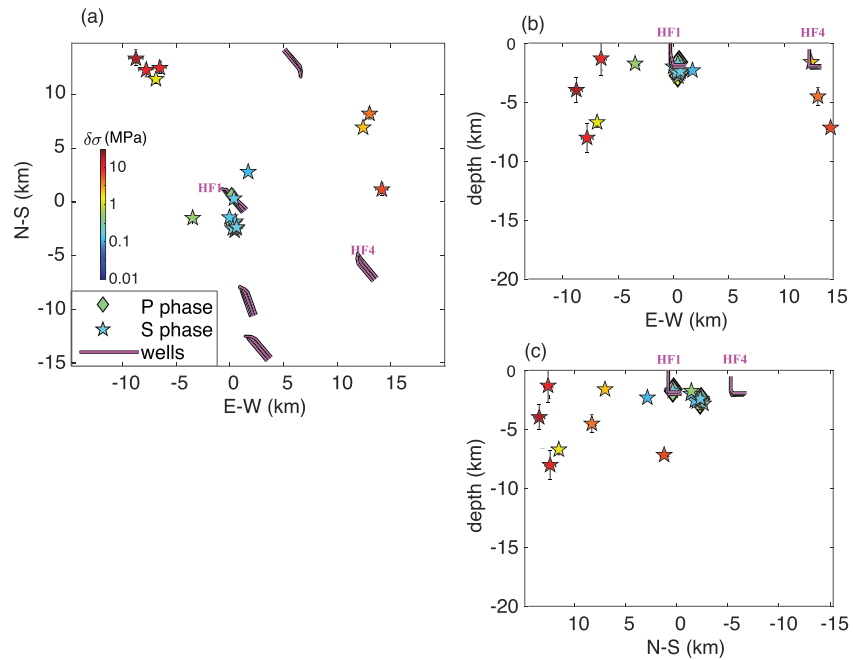


Figure 8. (a) Map view of the stress drop distribution based on spectral ratio estimates. Stars indicate the hypocenter locations of stress drop values estimated from *P/S* phases, with colorbar indicating the stress drop value in MPa. Pink lines: map view of the horizontal well trajectories. (b and c) Same as (a) but for E-W and N-S profiles, respectively. Hypocenters are from the relocated catalog by Yu et al. (2019).

Events proximal to HF1 (C1 and C2) have a roughly constant stress drop values of ~ 1 MPa, whereas events at greater distances have stress drop values of ~ 10 MPa. Both groups show a scattered scaling relationship with seismic moment, although within a limited, and largely nonoverlapping, magnitude range. All the events with smaller stress drop values are located at distances of ~ 2 km or less to the well HF1, and the distal events have higher stress drops (Figure 8a). Also, all the events proximal to HF1 are shallow (in sedimentary layers) whereas those at greater distances to the well extend over a broader depth distribution, down to ~ 8 km (Figures 8b and 8c).

3.3. Comparison Between Clustered-Q Single Spectrum and Spectra-Ratio Fitting

Our comparison focuses on the *S* phase estimates, given that the constrained spectra-ratio fits based on *P* phase limited. As shown in Figure 7, for earthquakes that are analyzed by both methods, stress drop values estimated from spectral ratio fitting are on average ~ 1.4 orders of magnitude higher than estimates from clustered-Q single spectrum fitting. This systematic discrepancy between estimates likely results from path and site effects that remain uncorrected in single spectrum fitting, which has been seen in many previous studies (e.g., Ide et al., 2003; Kwiatek et al., 2014; Viegas et al., 2010). For example, since we use a constant *Q* assumption for single spectrum fitting, the geometrical attenuation is dependent on the frequency as an exponential shape $\propto e^{-\frac{\pi f t}{Q}}$ (Shearer, 2019). While in the real case, the *Q* factor is also frequency dependent. Despite using a good overall estimate of the apparent *Q* value (i.e., optimal *Q*), we suspect that the real attenuation below 20 and 6 Hz is actually stronger than calculated attenuation for proximal and distal clusters, respectively. Thus, a lower corner frequency value would be expected in single spectrum estimates. Sumy et al. (2017) found much lower stress drops for the Prague sequence by fitting for *Q* and f_c , compared to later studies that used spectral ratios (Boyd et al., 2017; Huang et al., 2017). Even in relatively clean deep borehole recordings, Ide et al. (2003) show similarly that propagation effects could lead to more than a factor of 2 difference between corner frequency estimates from single spectrum versus spectral ratio fitting. The corner frequency differences would also lead to stress drop values more than 1 order of magnitude lower when estimated from single spectra. Therefore, we consider the spectral ratio fitting results as the most robust corner frequency and stress drop estimates. The clustered-Q spectra fitting results with a larger

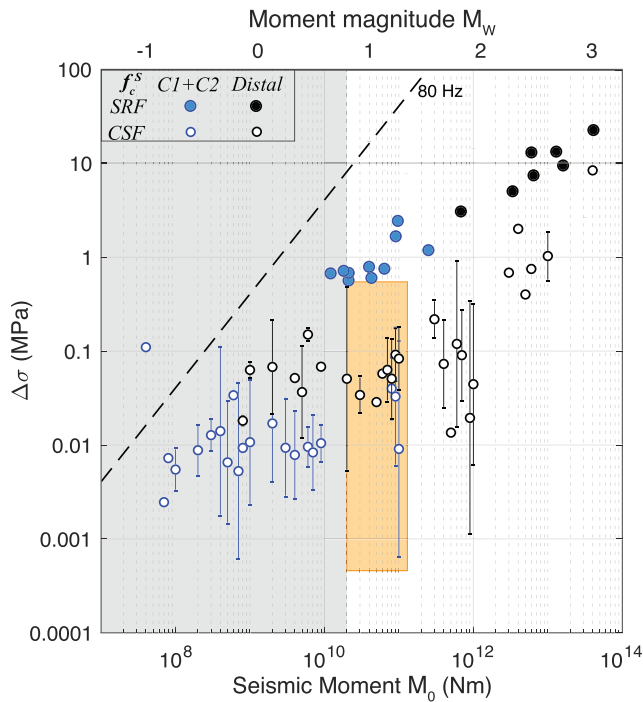


Figure 9. Stress drop scaling comparison between spectral ratio fitting (SRF) and clustered-Q spectra fitting (CSF), estimated based on *S* phase. Blue/black filled dots: stress drop of events proximal/distal to HF1 with SRF estimates. Blue/black empty dots: stress drop of proximal/distal groups with CSF estimates, averaged in $0.1 \times \log_{10}(M_0)$ bins with error bars indicating standard error. Static stress drop value estimates are calculated using a depth-dependent shear wave velocity. Gray shaded area: unreliable fits of events with $M_0 < 2 \times 10^{10}$ Nm ($M_W < 0.8$). Orange shaded area: highlights that the moment of CSF constrained events proximal and distal to the well only overlap in a narrow range of 2×10^{10} – 10^{11} Nm.

larger than the observed values in cases with more robustly constrained optimal apparent *Q* values (Figures 2c–2e). By contrast, the unanticipated values of theoretical apparent *Q* in some cases, either smaller or larger than the observed optimal apparent *Q* for distal groups (G4–G6), are probably due to the poor constraint of optimal *Q* (Figures 2b, 2f, and 2g). Although we do not obtain reliable estimates for all three layers exclusively based on *P* or *S* phases, the combination of good estimates from both phases helps prove the difference between the theoretical and observed apparent *Q* values at greater distance. The assumption of a true *Q* value being constant with horizontal distance to the well is unable to fully justify the observed difference between the apparent *Q* values at varying distances. Therefore, we infer that the true *Q* value is indeed larger at greater distances to the well.

4. Implication and Discussion

In our study, the stress drop values of IIEs in the proximity of the wellbore HF1 is lower relative to those at greater distances, that is, ~ 1 MPa versus ~ 10 MPa, based on the *S* phase spectral ratio estimations. The difference of absolute stress drop values could vary depending on the approach used to estimate them as well as the phases. For example, stress drop values would be lower from *S* phase clustered-Q spectral estimations (Figure 7). However, the relative difference between the stress drop estimates of the two clusters is visible regardless which method is used, suggesting that it is more reliable than the absolute values. In addition, a change in stress drop values for events above and below $M_W 2$ is also suggested by the spectral ratio estimates (Figure 9). Three possibilities may explain the observations: (i) The stress drop is relatively lower in close proximity to the wellbore due to the elevated pore pressure and/or rock damage, (ii) the stress drop scales with magnitude, or (iii) the low f_c value of small events near the wellbore could be a biased selection due to the limited frequency resolution. Ideally, the best way to identify which possibility is more dominant

number of resolved events are complementary to the spectral ratio fits. Albeit the absolute values of source parameters are less well-constrained compared to spectral ratio estimates, the stress drop scaling based on the clustered-*Q* spectra fits still holds. As Figure 9 shows, the overall trend can be consistently recognized that stress drop values observed for events close to the HF1 are relatively smaller compared to events more distal to the well. The difference in stress drop values between the proximal and distal populations can be easily recognized from spectral ratio fitting (blue and black solid circles), and results derived from clustered-*Q* spectrum fitting in the moment range of $\sim 2 \times 10^{10}$ – 10^{11} Nm ($M_W 0.8$ – 1.3 ; orange box) also agree with the stress drop difference. The $\Delta\sigma$ versus M_0 plot based on *P* phase estimates is available in Figure S4. The contrast in stress drop between proximal and distal event groups is less distinct compared with *S* phase due to a lack of robust estimations for distal events.

When using the *S* phase corner frequency values estimated from spectral ratio fittings to check the robustness of apparent *Q* value constrained by clustered-*Q* spectral fitting, we are able to establish 26 master-event pairs recorded by the same station. As a result, the averaged RMS misfit between the observed residual spectra ratio and the calculated geometrical spreading factor is 0.21, suggesting reliable estimations of the apparent *Q* values.

3.4. Spatial Variation of True *Q* Value

In order to reject the null hypothesis that the true *Q* value is invariant with respect to the distance to the well, we conduct a test assuming that the true *Q* value at distal distances is the same as in the proximity of the HF1.

The test results are marked as stars outlined in gray in Figures 2b–2g. The theoretical apparent *Q* values for Groups 4–6 are generally smaller

would be to quantify the trend in stress drop values over a wider range of magnitudes (e.g., Abercrombie & Rice, 2005; Ide et al., 2003). However, the events in close proximity to HF1 are nearly exclusively smaller than $M_W 2$. Conversely, we can also look at the corner frequency values of smaller magnitude events at larger distances, but their corner frequencies cannot be well constrained by the spectral ratio estimates due to their lower SNRs. We do observe differences in stress drop between the proximal and distal event clusters, albeit overlying for a limited magnitude range of $M_W 0.8$ – 1.3 (Figure 9). It would be less convincing to simply extrapolate to the whole magnitude range. Without larger events near the wellbore or spectral-ratio estimates for smaller events at greater distance, we are unable to confirm possibilities as (1) pore pressure and/or rock damage near the wellbore is responsible for lower stress drop values or (2) if there is indeed a scaling with magnitude.

There is also possibility that we miss source parameters for small earthquakes near the injection well with higher stress drop (i.e., higher f_c) because of the limited frequency range resolution (Shearer et al., 2019). For instance, if small events ($M < 2$) with stress drop ~ 10 MPa do exist near the wellbore, the corresponding f_c could have reached our frequency resolution ($f_{res} = 80$ Hz). In the case where f_c exceeds $1/2$ to $2/3$ of f_{res} (40–53 Hz), the f_c estimates would be biased low (Abercrombie et al., 2017; Ruhl et al., 2017). Admittedly, the effective way to resolve such a question is to record more earthquakes in a longer observational period or to improve the frequency resolution with higher sample-rate seismometers. However, the consistent facts that (1) none of the constrained S phase single spectrum estimates exceeds $1/2f_{res}$ (Figure 6) and (2) the spectral-ratio estimates are all below $2/3f_{res}$, with only one falling in the ambiguous range of $1/2f_{res} < f_c < 2/3f_{res}$ but still following the 1 MPa stress drop scaling (Figure 7), may instead suggest that the possibility of selection bias related to proximal small events is unlikely the main factor leading to the spatial variation of stress drop.

Moreover, several lines of indirect evidence support the hypothesis that the stress drop is lower near the well. First, if we consider the resolved events in two groups: proximal (clusters C1 and C2) and distal (others) to the well, the stress drop values of events in each group are roughly invariant relative to seismic moment (Figure 7), although the range of magnitudes is small and nonoverlapping. In other words, the stress drop values vary negligibly within individual groups of earthquakes proximal or distal to the well. It is sufficient to prove that the stress drop difference between two groups is statistically significant. Additionally, the poroelastic modeling results of Yu et al. (2019) suggest that the pore pressure change within 1 km of the well could reach several MPa, as opposed to a very limited stress change inferred at distances greater than 5 km ($\sim 10^{-3}$ MPa). The modeled stress changes would be one of significant factors to explain the differences in observed stress drop values between proximal and distal event groups here in the context of a Mohr-Coulomb failure criterion. Since pore pressure perturbations would not be expected to be high immediately following the start of injection activity, it may alternatively explain why larger-magnitude HF IIE occur at distances beyond ~ 1 km of the well with a time delay. Another possible scenario is that the fault shear strength near the well bore could be relatively lower compared to greater distances, considering hydraulic stimulation increases fluid pressure and fracture density near the well bore, the latter is shown to lead to lower equivalent friction coefficient for fractured rock masses (Zhang & Sanderson, 2001). That is, injection likely facilitates the occurrence of proximal events with lower stress drop values that presumably result from possible slower ruptures in the damaged rocks near the wellbore compared to the more intact rock away from it. Similar spatial pattern of stress drop increase is also valid for IIE sequence near Crooked Lake, Alberta, in the context of distance range within several kilometers (Clerc et al., 2016). Goertz-Allmann et al. (2011) and Kwiitek et al. (2014) also report stress drop increase with distance to the well at the Basel geothermal site and Berlin geothermal field, respectively, although both observations only cover spatial distance up to hundreds of meters. Specifically, Kwiitek et al. (2014) show a gradual stress drop increase from ~ 1 to ~ 10 MPa in a distance range of 100–500 m from the injection well, using borehole seismometers with sample-rate up to 3,000 Hz. Conversely, Trugman et al. (2017) reported no relation between distance and stress drop of WD induced earthquakes in southern Kansas. Such findings, however, are not contradictory to the findings in this study, because WD injection is pervasive in Kansas and hence widespread elevation of pore pressures is expected, as opposed to an isolated HF wells with associated seismicity.

Furthermore, a relatively lower true Q value near the well suggests a higher degree of rock damage and potentially higher pore fluid pressures related to HF injection (Worthington & Hudson, 2000). The

variation of true Q thus provides independent evidence to support an interpretation of the stress drop difference as a manifestation of rock strength difference between the proximal and distal events. Joint constraints from stress drop and Q -value distributions also provide a more comprehensive understanding of the distance-decaying influence associated with HF fluid injection.

Before making a direct comparison between our stress drop estimates and that from other studies, a number of model dependent features need to be considered (Kaneko & Shearer, 2015). First, we use the k factor by Sato and Hirasawa (1973) in the stress drop calculation (Equation 6), which leads to considerable differences between our values and those derived with other models. For example, our stress drop values are only 30% of the Madariaga stress drop (Madariaga, 1976) and 160% of the Brune stress drop (Brune, 1970), given the same velocity model. Second, induced earthquakes might have nonnegligible nondouble-couple (non-DC) components, which could bias the moment estimates (Zhang et al., 2016). The adjusted seismic moment (M_0) of the proximal events (clusters C1 and C2) would be corrected to 49% and 54% of their pure-DC values for P and S phase, respectively (Figure S5 and Text S2). The corrected stress drop values would still be proportionally lower with less discrepancy between values derived from P and S phases, but the scaling remains the same (Figure S6). While the Brune model derived from a flat circular shear crack model (Brune, 1970, 1971) would be insufficient in describing the source parameters of earthquakes with nonnegligible non-DC components and thus potentially affects the corner frequency estimations (e.g., Liu et al., 2020), we note that recent work by Roth et al. (2020) and references therein point to induced earthquake in the region being consistent with shear reactivation of existing faults correlated with injection activity.

Third, it is necessary to consider the possible influence of an overestimated seismic velocity near the HF well on the static stress drop ($\Delta\sigma$), where $\Delta\sigma \propto c_s^{-3}$ (Eshelby, 1957). High-rate fluid injection could result in a lower seismic velocity surrounding the well by increasing fracture density and decreasing the effective stress through increased pore pressure. Also, the $Q_p/Q_s < 1$ near HF1 suggests hydrocarbon saturation (Klimentos, 1995; Maultzsch et al., 2003), indicating a reduced seismic (particularly S wave) velocity near the well bore relative to the regional 1-D velocity model. If a velocity contrast indeed exists between the volume near HF1 and at greater distances to fully address the differences in stress drop values, we can speculate c_s close to the well would need to be reduced by 46%. Even if such high variation in shear wave velocity is possible, the highly fractured volume due to HF injection should be very limited, perhaps no more than 200 m from the wellbore. On the other hand, the low seismic injection efficiency (the ratio of cumulative radiated energy of IIE and hydraulic energy in a certain time period) in the Montney shale formation indirectly suggests a low radiation efficiency of earthquake sources (Maxwell et al., 2018), indicating a low rupture velocity (Husseini & Randall, 1976). However, such low rupture velocity is expected to equally affect both the proximal and distal clusters. Therefore, velocity overestimation, either due to the HF related higher fracture density or the sedimentary geological setting, is unlikely the leading factor of the stress drop difference between proximal and distal events. The observed variation probably results from additional factors, such as elevated fluid pressure, which helps justify the applied 1-D layered velocity model.

5. Conclusion

We investigate the source parameters of 484 events (M_W -1.0 to 3.0) that occurred between 28 May and 15 October 2015 surrounding a hydraulic fracturing well in northeast British Columbia. Spectral ratio fitting implies that static stress drop values fall in the range of 0.7–21.9 MPa, typical of tectonic earthquakes. Both the spectral ratio fitting for limited event pairs and a clustered- Q single spectral fitting for a larger number of events consistently suggest a stress drop difference between clusters proximal and distal to the well; earthquakes within ~ 2 km of the active HF well have lower stress drop values (~ 0.1 –1 MPa) relative to earthquakes at greater distance (~ 1 –10 MPa). The stress drop values of either cluster are roughly invariant with seismic moment, although within a limited, and non-overlapping magnitude range. Due to the lack of larger-magnitude events near the borehole and robust spectral-ratio estimates for smaller events at greater distance, we are unable to definitively exclude the possibility that stress drop scales with magnitude, which is commonly observed for earthquakes of such small magnitudes and often attributed to an observational artifact. Nevertheless, estimates of seismic attenuation factor Q based on the single spectrum fitting also suggest lower Q proximal to the well. The combination of low stress drop values and low seismic Q probably imply that the higher fracture density and/or elevated pore pressures near the well prevent the crustal

rocks from storing and releasing larger magnitudes of stress compared to ostensibly less damaged rock at greater distances. The observations presented here support the interpretation of a heterogeneous stress state near the well and may provide an explanation for why larger-magnitude HF IIEs occur at distances beyond ~1 km of the well with a time delay, where pore pressure perturbations would not be expected to be high immediately following the start of injection activity.

Data Availability Statement

Waveform data is available through Yu et al. (2019). Well data are publicly available from the British Columbia Oil and Gas Commission database. A catalog containing all relevant source parameters and their uncertainties is available at <https://doi.org/10.5281/zenodo.3905328> (<https://zenodo.org/record/3905329#.XxHwTZNKjBI>).

Acknowledgments

We appreciate the two anonymous reviewers and Yihe Huang for their constructive reviews. We thank Conan Drummond for his help in the deployment of seismic stations, as well as Mark Norton from Progress Energy for assistance in collecting the waveform data, and the BC Oil and Gas Commission for providing HF well injection data (<https://www.bcogc.ca/data-reports/data-centre/>). This work is supported in part by the Canadian Foundation for Innovation LOF fund 32840, new faculty startup funds from the Ruhr University Bochum, the Natural Sciences and Engineering Research Council of Canada Strategic Grant: STPGP/494141-2016, the NRCan Energy Innovation Program, the GSC Environmental Geoscience Program, and Geoscience BC fund 2019-007a. This paper is NRCan contribution 20200095.

References

- Abercrombie, R. (1995). Earthquake source scaling relationships from -1 to 5 ML using seismograms recorded at 2.5 km depth. *Journal of Geophysical Research*, *100*(B12), 24,015–24,036.
- Abercrombie, R., & Leary, P. (1993). Source parameters of small earthquakes recorded at 2.5 km depth, Cajon Pass, southern California: Implications for earthquake scaling. *Geophysical Research Letters*, *20*(14), 1511–1514. <https://doi.org/10.1029/93GL00367>
- Abercrombie, R. E. (1997). Near-surface attenuation and site effects from comparison of surface and deep borehole recordings. *Bulletin of the Seismological Society of America*, *87*(3), 731–744.
- Abercrombie, R. E. (2015). Investigating uncertainties in empirical Green's function analysis of earthquake source parameters. *Journal of Geophysical Research: Solid Earth*, *120*, 4263–4277. <https://doi.org/10.1002/2015JB011984>
- Abercrombie, R. E., Bannister, S., Ristau, J., & Doser, D. (2017). Variability of earthquake stress drop in a subduction setting, the Hikurangi Margin, New Zealand. *Geophysical Journal International*, ggw393.
- Abercrombie, R. E., & Rice, J. R. (2005). Small earthquake scaling revisited: Can it constrain slip weakening? *Geophysical Journal International*, *162*(2), 406–424. <https://doi.org/10.1111/j.1365-246X.2005.02579.x>
- Aki, K., & Richards, P. (1980). *Quantitative seismology* (p. 932). New York: W. H. Freeman. <https://doi.org/10.1121/1.385057>
- Boyd, O. S., McNamara, D. E., Hartzell, S., & Choy, G. (2017). Influence of lithostatic stress on earthquake stress drops in North America. *Bulletin of the Seismological Society of America*, *107*(2), 856–868. <https://doi.org/10.1785/0120160219>
- Brune, J. N. (1970). Tectonic stress and seismic shear waves from earthquakes. *Journal of Geophysical Research*, *75*(26), 4997–5009. <https://doi.org/10.1029/JB075i026p04997>
- Brune, J. N. (1971). Seismic sources, fault plane studies and tectonics. *Eos, Transactions American Geophysical Union*, *52*(5), IUGG-178.
- Chen, X., & Shearer, P. M. (2013). California foreshock sequences suggest aseismic triggering process. *Geophysical Research Letters*, *40*, 2602–2607. <https://doi.org/10.1002/grl.50444>
- Clerc, F., Harrington, R. M., Liu, Y., & Gu, Y. J. (2016). Stress drop estimates and hypocenter relocations of induced seismicity near Crooked Lake, Alberta. *Geophysical Research Letters*, *43*, 6942–6951. <https://doi.org/10.1002/2016GL069800>
- Ellsworth, W. L. (2013). Injection-Induced Earthquakes. *Science*, *341*(6142), 1225942–1225942. <https://doi.org/10.1126/science.1225942>
- Eshelby, J. D. (1957). The determination of the elastic field of an ellipsoidal inclusion, and related problems. *Proceedings of the Royal Society of London A*, *241*(1226), 376–396.
- Fasola, S. L., Brudzinski, M. R., Skoumal, R. J., Langenkamp, T., Currie, B. S., & Smart, K. J. (2019). Hydraulic fracture injection strategy influences the probability of earthquakes in the Eagle Ford shale play of South Texas. *Geophysical Research Letters*, *46*, 12958–12967. <https://doi.org/10.1029/2019GL085167>
- Fehler, M., & Phillips, W. S. (1991). Simultaneous inversion for Q and source parameters of microearthquakes accompanying hydraulic fracturing in granitic rock. *Bulletin of the Seismological Society of America*, *81*, 553–575.
- Goertz-Allmann, B. P., Goertz, A., & Wiemer, S. (2011). Stress drop variations of induced earthquakes at the Basel geothermal site. *Geophysical Research Letters*, *38*, L09308. <https://doi.org/10.1029/2011GL047498>
- Hanks, T. C. (1979). b values and $\omega^{-\gamma}$ seismic source models: Implications for tectonic stress variations along active crustal fault zones and the estimation of high-frequency strong ground motion. *Journal of Geophysical Research*, *84*, 2235–2242.
- Holmgren, J. M., Atkinson, G. M., & Ghofrani, H. (2019). Stress drops and directivity of induced earthquakes in the western Canada sedimentary basin. *Bulletin of the Seismological Society of America*, *109*(5), 1635–1652. <https://doi.org/10.1785/0120190035>
- Hough, S. E. (2014). Shaking from injection-induced earthquakes in the central and eastern United States. *Bulletin of the Seismological Society of America*, *104*(5), 2619–2626. <https://doi.org/10.1785/0120140099>
- Hough, S. E., & Dreger, D. S. (1995). Source parameters of the 23 April 1992 M 6.1 Joshua Tree, California, earthquake and its aftershocks: Empirical Green's function analysis of GEOS and TERRAScope data. *Bulletin of the Seismological Society of America*, *85*(6), 1576–1590.
- Huang, Y., Beroza, G. C., & Ellsworth, W. L. (2016). Stress drop estimates of potentially induced earthquakes in the Guy-Greenbrier sequence. *Journal of Geophysical Research: Solid Earth*, *121*, 6597–6607. <https://doi.org/10.1002/2016JB013067>
- Huang, Y., De Barros, L., & Cappa, F. (2019). Illuminating the rupturing of microseismic sources in an injection-induced earthquake experiment. *Geophysical Research Letters*, *46*, 9563–9572. <https://doi.org/10.1029/2019GL083856>
- Huang, Y., Ellsworth, W. L., & Beroza, G. C. (2017). Stress drops of induced and tectonic earthquakes in the central United States are indistinguishable. *Science Advances*, *3*(8), p.e1700772.
- Husseini, M. I., & Randall, M. J. (1976). Rupture velocity and radiation efficiency. *Bulletin of the Seismological Society of America*, *66*(4), 1173–1187.
- Ide, S., Beroza, G. C., Prejean, S. G., & Ellsworth, W. L. (2003). Apparent break in earthquake scaling due to path and site effects on deep borehole recordings. *Journal of Geophysical Research*, *108*(B5), 2271. <https://doi.org/10.1029/2001JB001617>
- Imanishi, K., Takeo, M., Ellsworth, W. L., Ito, H., Matsuzawa, T., Kuwahara, Y., et al. (2004). Source parameters and rupture velocities of microearthquakes in Western Nagano, Japan, determined using stopping phases. *Bulletin of the Seismological Society of America*, *94*(5), 1762–1780. <https://doi.org/10.1785/012003085>

- International Seismological Centre (2019). *On-line Bulletin*. Thatcham, UK: International Seismology Centre. <http://www.isc.ac.uk>
- Kanamori, H. (1978). Quantification of earthquakes. *Nature*, 271(5644), 411.
- Kaneko, Y., & Shearer, P. M. (2015). Variability of seismic source spectra, estimated stress drop, and radiated energy, derived from cohesive-zone models of symmetrical and asymmetrical circular and elliptical ruptures. *Journal of Geophysical Research: Solid Earth*, 120, 1053–1079. <https://doi.org/10.1002/2014JB011642>
- Klimentos, T. (1995). Attenuation of P- and S-waves as a method of distinguishing gas and condensate from oil and water. *Geophysics*, 60(2), 447–458. <https://doi.org/10.1190/1.1443782>
- Ko, Y.-T., Kuo, B.-Y., & Hung, S.-H. (2012). Robust determination of earthquake source parameters and mantle attenuation. *Journal of Geophysical Research*, 117, B04304. <https://doi.org/10.1029/2011JB008759>
- Kwiatk, G., Bulut, F., Bohnhoff, M., & Dresen, G. (2014). High-resolution analysis of seismicity induced at Berlin geothermal field, El Salvador. *Geothermics*, 52, 98–111. <https://doi.org/10.1016/j.geothermics.2013.09.008>
- Laske, G., Masters, G., Ma, Z., & Pasyanos, M. (2013). Update on CRUST1. 0-A 1-degree global model of Earth's crust. *Paper presented at EGU General Assembly*, Vienna, Austria.
- Lei, X., Wang, Z., & Su, J. (2019). The December 2018 ML 5.7 and January 2019 ML 5.3 earthquakes in South Sichuan Basin induced by shale gas hydraulic fracturing. *Seismological Research Letters*, 90(3), 1099–1110. <https://doi.org/10.1785/0220190029>
- Liu, M., Huang, Y., & Ritsema, J. (2020). Stress drop variation of deep-focus earthquakes based on empirical Green's functions. *Geophysical Research Letters*, 47, e2019GL086055. <https://doi.org/10.1029/2019GL086055>
- Madariaga, R. (1976). Dynamics of an expanding circular crack. *Bulletin of the Seismological Society of America*, 66, 639–666.
- Mahani, A. B., Schultz, R., Kao, H., Walker, D., Johnson, J., & Salas, C. (2017). Fluid injection and seismic activity in the northern Montney play, British Columbia, Canada, with special reference to the 17 August 2015 Mw 4.6 induced earthquake. *Bulletin of the Seismological Society of America*, 107(2), 542–552. <https://doi.org/10.1785/0120160175>
- Maultzsch, S., Chapman, M., Liu, E., & Li, X. Y. (2003). Modelling frequency-dependent seismic anisotropy in fluid-saturated rock with aligned fractures: Implication of fracture size estimation from anisotropic measurements. *Geophysical Prospecting*, 51(5), 381–392. <https://doi.org/10.1046/j.1365-2478.2003.00386.x>
- Maxwell, S. C., Garrett, D., Huang, J., & Mamer, P. (2018). Monitoring of induced seismicity associated with hydraulic fracturing in the Montney shale. In 52nd US Rock Mechanics/Geomechanics Symposium. American Rock Mechanics Association.
- Mori, J., & Frankel, A. (1990). Source parameters for small events associated with the 1986 North Palm Springs, California, earthquake determined using empirical green functions. *Bulletin of the Seismological Society of America*, 80(2), 278–295.
- Roth, M. P., Verdecchia, A., Harrington, R. M., & Liu, Y. (2020). High-resolution imaging of hydraulic-fracturing-induced earthquake clusters in the Dawson-Septimus Area, Northeast British Columbia, Canada. *Seismological Research Letters*, 1–13. <https://doi.org/10.1785/02202000086>
- Ruhl, C. J., Abercrombie, R. E., & Smith, K. D. (2017). Spatiotemporal variation of stress drop during the 2008 Mogul, Nevada, earthquake swarm. *Journal of Geophysical Research: Solid Earth*, 122, 8163–8180. <https://doi.org/10.1002/2017JB014601>
- Sato, T., & Hirasawa, T. (1973). Body wave spectra from propagating shear cracks. *Journal of Physics of the Earth*, 21(4), 415–431. <https://doi.org/10.4294/jpe1952.21.415>
- Satoh, T. (2006). Influence of fault mechanism, depth, and region on stress drops of small and moderate earthquakes in Japan. *Structural Engineering/Earthquake Engineering*, 23(1), 125s–134s.
- Scholz, C. (2019). *The mechanics of earthquakes and faulting* (p. 471). Cambridge: Cambridge Univ. press. <https://doi.org/10.1017/9781316681473>
- Schultz, R., Corlett, H., Haug, K., Kocon, K., Mac Cormack, K., Stern, V., & Shipman, T. (2016). Linking fossil reefs with earthquakes: Geologic insight to where induced seismicity occurs in Alberta. *Geophysical Research Letters*, 43, 2534–2542. <https://doi.org/10.1002/2015GL067514>
- Schultz, R., Skoumal, R. J., Brudzinski, M. R., Eaton, D., Baptie, B., & Ellsworth, W. (2020). Hydraulic fracturing induced seismicity. *Reviews of Geophysics*, 58, e2019RG000695. <https://doi.org/10.1029/2019RG000695>
- Shearer, P. M. (2019). *Introduction to seismology* (p. 263). Cambridge: Cambridge university press.
- Shearer, P. M., Abercrombie, R. E., Trugman, D. T., & Wang, W. (2019). Comparing EGF methods for estimating corner frequency and stress drop from P wave spectra. *Journal of Geophysical Research: Solid Earth*, 124, 3966–3986. <https://doi.org/10.1029/2018JB016957>
- Shi, J., Kim, W.-Y., & Richards, P. (1998). The corner frequency and stress drops of intraplate earthquakes in the northeastern United States. *Bulletin of the Seismological Society of America*, 88, 531–542.
- Sumy, D. F., Neighbors, C. J., Cochran, E. S., & Keranen, K. M. (2017). Low stress drops observed for aftershocks of the 2011 Mw 5.7 Prague, Oklahoma, earthquake. *Journal of Geophysical Research: Solid Earth*, 122, 3813–3834. <https://doi.org/10.1002/2016JB013153>
- Thomson, D. J. (1982). Spectrum estimation and harmonic analysis. *Proceedings of the IEEE*, 70(9), 1055–1096. <https://doi.org/10.1109/PROC.1982.12433>
- Toksöz, M. N., Johnston, D. H., & Timur, A. (1979). Attenuation of seismic waves in dry and saturated rocks: I. Laboratory measurements. *Geophysics*, 44(4), 681–690. <https://doi.org/10.1190/1.1440969>
- Tomic, J., Abercrombie, R. E., & do Nascimento, A. F. (2009). Source parameters and rupture velocity of small $M \leq 2.1$ reservoir induced earthquakes. *Geophysical Journal International*, 179(2), 1013–1023. <https://doi.org/10.1111/j.1365-246X.2009.04233.x>
- Trugman, D. T., Dougherty, S. L., Cochran, E. S., & Shearer, P. M. (2017). Source spectral properties of small to moderate earthquakes in southern Kansas. *Journal of Geophysical Research: Solid Earth*, 122, 8021–8034. <https://doi.org/10.1002/2017JB014649>
- van der Elst, N. J., Page, M. T., Weiser, D. A., Goebel, T. H. W., & Hosseini, S. M. (2016). Induced earthquake magnitudes are as large as (statistically) expected. *Journal of Geophysical Research: Solid Earth*, 121, 4575–4590. <https://doi.org/10.1002/2016JB012818>
- Viegas, G., Abercrombie, R. E., & Kim, W.-Y. (2010). The 2002 M5 Au Sable Forks, NY, earthquake sequence: Source scaling relationships and energy budget. *Journal of Geophysical Research*, 115, B07310. <https://doi.org/10.1029/2009JB006799>
- Visser, R., Smith, B., Kao, H., Babaie Mahani, A., Hutchinson, J., & McKay, J. E. (2017). A comprehensive earthquake catalogue for northeastern British Columbia and western Alberta, 2014–2016. *Geological Survey of Canada Open-File Report*, 8335, 27. <https://doi.org/10.4095/306292>
- Wang, B., Harrington, R. M., Liu, Y., Kao, H., & Yu, H. (2020). A study on the largest hydraulic fracturing induced earthquake in Canada, Part 1: Observations and static stress drop estimation. *Bulletin of the Seismological Society of America*. <https://doi.org/10.1785/0120190261>
- Worthington, M. H., & Hudson, J. A. (2000). Fault properties from seismic Q. *Geophysical Journal International*, 143(3), 937–944. <https://doi.org/10.1046/j.1365-246X.2000.00315.x>

- Ye, Z., & Ghassemi, A. (2018). Experimental study on injection-induced fracture propagation and coalescence for EGS stimulation. *Paper presented at the 43rd Workshop on Geothermal Reservoir Engineering*, Stanford, CA.
- Yu, H., Harrington, R. M., Liu, Y., & Wang, B. (2019). Induced seismicity driven by fluid diffusion revealed by a near-field hydraulic stimulation monitoring array in the Montney Basin, British Columbia. *Journal of Geophysical Research: Solid Earth*, *124*, 4694–4709. <https://doi.org/10.1029/2018JB017039>
- Zhang, H., Eaton, D. W., Li, G., Liu, Y., & Harrington, R. M. (2016). Discriminating induced seismicity from natural earthquakes using moment tensors and source spectra. *Journal of Geophysical Research: Solid Earth*, *121*, 972–993. <https://doi.org/10.1002/2015JB012603>
- Zhang, X., & Sanderson, D. J. (2001). Evaluation of instability in fractured rock masses using numerical analysis methods: Effects of fracture geometry and loading direction. *Journal of Geophysical Research*, *106*(B11), 26,671–26,687. <https://doi.org/10.1029/2001JB000311>